Heliyon 5 (2019) e01716

Contents lists available at ScienceDirect

Heliyon

journal homepage: www.heliyon.com

Synthesis and characterization of Zn-Doped hydroxyapatite: scaffold application, antibacterial and bioactivity studies

Edwin Andrew Ofudje [a,b,*], Abideen Idowu Adeogun [b], Mopelola Abidemi Idowu [b], Sarafadeen Olateju Kareem [c]

[a] Department of Chemical Sciences, Mountain Top University, Ibafo, Nigeria
[b] Department of Chemistry, Federal University of Agriculture, Abeokuta, Nigeria
[c] Department of Microbiology, Federal University of Agriculture, Abeokuta, Nigeria

ARTICLE INFO

Keywords:
Materials science
Materials chemistry

ABSTRACT

In this study, the antimicrobial and scaffold of zinc-substituted hydroxyapatite, (Zn-HAp) synthesized via chemical co-precipitation technique was investigated. The structure of the synthesized Zn-HAp was investigated with X-ray diffraction (XRD), Fourier transform infrared (FT-IR) spectroscopy, Scanning electron microscope (SEM), Energy dispersive X-spectroscopy (EDAX), transmission electron microscope (TEM), Thermogravimetric analysis (TGA) and X-ray photoelectron spectroscopy (XPS). Bioactivity study was performed in simulated body fluid (SBF), while the antimicrobial activity was studied using disc diffusion method. The XRD structure revealed that Zn ion incorporation up to 10% led to the second phase hydroxyapatite (HAp) formation, while higher concentration diminished the apatite structure. The presence of phosphate ions, carbonates ions, and hydroxyl groups in the apatite powder was ascertained by the FT-IR evaluation. SEM evaluation showed that the apatite contains fine particles with nearly round shape with interconnected pores and decreasing Ca/P ratio with increasing Zn ion concentration. TEM results showed particulate polycrystalline apatite with crystallite size ranging from 68 nm in pure HAp to 41 nm in 20% Zn-doped HAp indicating a decrease in the crystal size with increasing Zn ion in the samples. The bioactivity study showed spherical deposition around the porous region of the scaffold HAp suggesting the growth of apatite in SBF media after 7 days of incubation, while antibacterial activity studies showed zones of inhibition with an increase in zinc ions concentrations.

1. Introduction

In recent years, hydroxyapatite (HAp) has gained much interest owing to the rising need for more biomaterials. Its role as an implant material and bone filler is due to its exceptional bioactivity, biocompatibility, osteoconductivity and crystallographic structure with similarity to the mineral segment of natural bone [1, 2, 3]. Chemically synthesized HAp shows resemblance in composition when compared with biological HAp and therefore can perform many properties of natural HAp such as the provision of the surface for the deposit of calcium-containing mineral during anchorage-dependent osteoblasts when used as an orthopedic or dental implant [1, 4]. Its osteoconductivity is as a result of its potentials to attach strongly with natural bone tissue and its ion-exchange ability against various cations makes it highly biocompatible with inherent bioactivity properties [4, 5].

Despite these important applications and optical properties of synthetic HAp, its use is impaired by poor mechanical properties such as low impact resistance and high solubility during in vivo applications. The formation of microbes at the sites of implantation is one of the major failures in the implantation process [6]. Another significant post-implantation problem noticed is the contamination by bacteria which is due to the colonization and adhesion on the surface of the biomaterials and is considered as an impediment of traumatology and orthopedics [7]. But with the implant materials having antimicrobial activity within their structures, this setback will be eliminated. To address these problems, materials such as polyethylene [8], Al_2O_3 [9], TiO_2 [10], Y_2O_3 [11] and carbon nanotubes [12] have been used to improve the mechanical properties of HAp. However, the micro-structural impact of the reinforcements on HAp is a major concern also, as its effect could weaken the biological property of HAp thus resulting in undesirable effects on the tissues [13].

Zn is a crucial element with many important biological roles and is

* Corresponding author.
E-mail addresses: ofudjeandrew4real@yahoo.com, ofudje@gmail.com (E.A. Ofudje).

https://doi.org/10.1016/j.heliyon.2019.e01716
Received 11 December 2018; Received in revised form 16 April 2019; Accepted 9 May 2019

responsible for regulating many enzymes activities and the uptake and release of Zn is strongly assisted by the bone reservoir in the body [14]. The natural HAp containing zinc is made up of biological tissues such as bone and enamel of human teeth. Bone formation and mineralization caused by the stimulatory effect of Zn has been reported [15, 16] and its implants incorporation has been shown to promotes the formation of bone around the implant which decreases the inflamatory response [15, 17]. The antibacterial and antifungal behaviour of Zn doped HAp has been studied [18] while its nano-rods are reported to have improved performance against oral cavity bacteria [19]. But the structural implication of the dopant has not been well reported.

This study focused on the micro-structural impact of Zn doping on the HAp, also, bioactivity and antimicrobial studies of HAp after the incorporation of zinc ions were also investigated. Different amount of zinc ions were doped with HAp via chemical co-precipitation method, while the microstructural changes were investigated by XRD, FT-IR, EDAX, SEM, TEM and XPS analytical techniques. Bioactivity and antimicrobial property of zinc-doped HAp were also reported.

2. Experimental

2.1. Synthesis of HAp and Zn-Doped HAp

Pure HAp and Zn-doped HAp were prepared by adopting the method described by Gross *et al.* [20] with slight modifications. An aqueous solution of 0.1 M $Ca(NO_3)_2 \cdot 6H_2O$ was prepared in 250 ml volumetric flask and stirred for 10 mins on a magnetic stirrer. An aqueous solution of 0.06 M $(NH_4)H_2PO_4$ was then added dropwise while the reaction was maintained at pH 11 using ammonia solution. The suspension was stirred for 24 hrs, centrifuged for 15 mins at 4000 rpm and washed several times using deionized water. The resulting precipitate sample was dried in an oven at 100 °C overnight. The experiment was repeated by using different concentrations of $Ca(NO_3)_2 \cdot 6H_2O$ (0.095, 0.090, 0.085 and 0.080 M) mixed with various concentrations of $Zn(NO_3)_2.6H_2O$ (0.005, 0.010, 0.015 and 0.02 M) to prepare Zn-HAp as 5, 10, 15 and 20 mol% zinc substituted hydroxyapatite and designated as 5%Zn + HAp, 10%Zn + HAp, 15%Zn + HAp and 20%Zn + HAP respectively. Scheme 1 summarizes the chemical synthesis of HAp.

2.2. Characterization

X-ray diffraction (XRD) of the prepared biomaterial was done using PANalytical (X'Pert PRO, Netherland) in the angle range of $2\theta = 10°–60°$ using CuKα ($\gamma = 1.54178$ Å) radiation. JCPDS files 09–432 was used to confirmed the various peaks developed in the apatite, while crystallite sizes were computed using the Debye-Scherrer equation [20] and the hexagonal crystal parameters were calculated from the equation of Bragg's reflection [21] and the volume (V) of the hexagonal unit cell of hydroxyapatite subsequently estimated [22]. Fourier Transform Infrared (FT-IR) spectroscopy was utilized to assess the various functional groups which are present on the biomaterials by using Bruker Optics, TENSOR 27 series FT-IR spectrometer. KBr pellets were made by mixing the HAp powder with KBr in the ratio of 1:99% using mortar and pestle and thereafter compressed to form the pellet. Spectra were recorded between the range of 4000 cm^{-1} to 400 cm^{-1} with a scan average of 64 at a resolution of 4 cm^{-1}. Elemental composition and the morphology of the HAp and Zn-doped HAp composite were evaluated with the aid of Energy Dispersive X-Spectroscopy (EDAX) (Hitachi, Japan, an S–3000H electron

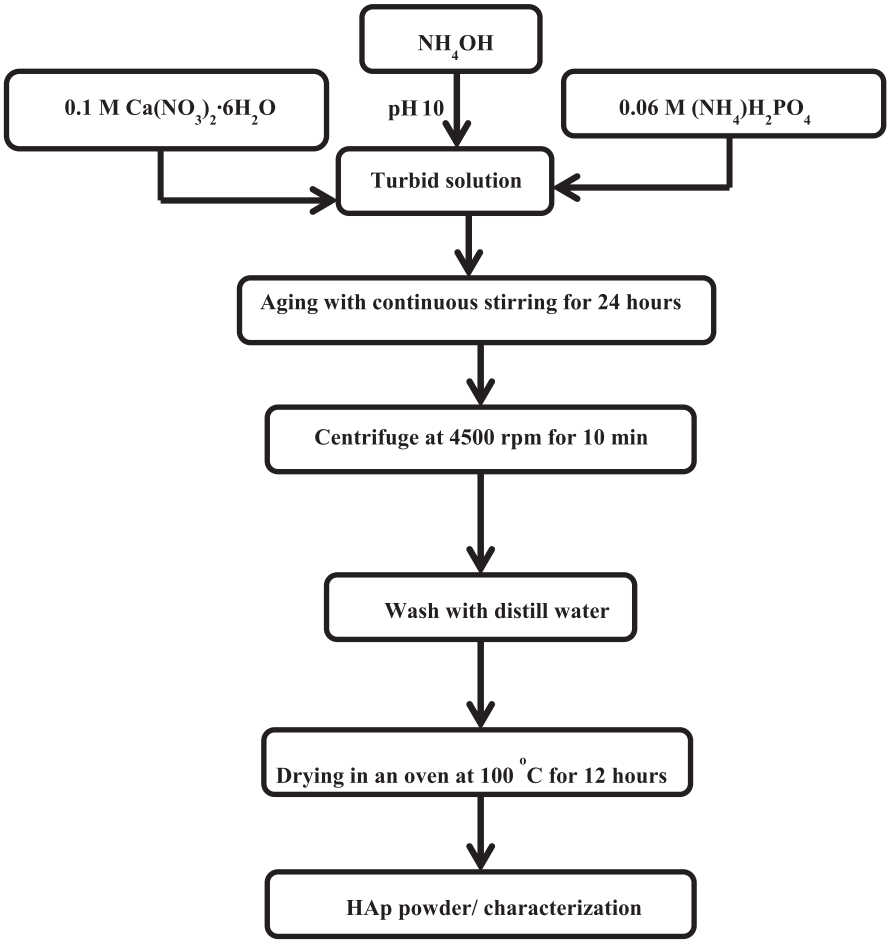

Scheme 1. Flow chart for the chemical synthesis of HAp.

microscope with an accelerating voltage of 15 kV). Detailed information about morphological and particle size measurement of as-prepared HAp powders was examined with a transmission electron microscope (TEM; Tecnai 20 G2 FEI, Netherland). Samples for TEM analysis were prepared by dispersing the particle in ultrapure water and sonicated for 15 mins. A drop of the dispersed particle was drop on the copper grid and allowed to dry under the infrared lamp before observation. X-ray photoelectron spectroscopy measurements were done with X-ray photoelectron spectroscopy (XPS, Thermo V G Scientific, UK) using monochromatic Al K as a source of radiation. A value of 45 was set as the X-ray photoelectron spectroscopy take-off angle, while Spectral Data Processor v2.3 (SDP) software was used to process the XPS spectra recorded. The thermal stability of pure HAp and Zn-doped HAp composite were performed using SDT Q600 V8.3 Build 101 simultaneous DSC-TGA instrument. The measurements were achieved between room temperature and 1000 °C with a heating rate of 5 °cm^{-1}. Universal V4.7A TA software package was utilized in the data analysis.

2.3. Scaffold preparations

HAp scaffold was made by adding calculated amount of Zn-doped-HAp powder with ammonium bicarbonate (AMB) which served as the pore-forming agent, while a hydraulic press was used to form the pellets at varying compaction pressure and calcined at 1000 °C in a box furnace to produce scaffold HAp. The surface morphology of the fabricated scaffold was examined by SEM, while the apatite porosity was assessed by a mercury porosimeter.

2.4. In vitro bioactivity study

Scaffold pellet was put in an abrade bottle filled with 150 ml simulated body fluid prepared as described by Kokubo and Takadama, [23]. The bottle was maintained at 37 °C in a water bath shaker. After 3–7 days of immersion, the specimens were removed, gently washed with distilled water and dried at room temperature. The surface morphologies of the pellet were investigated with SEM, while the functional groups were examined with FT-IR analysis.

2.5. Antibacterial study

Two different bacteria namely: *Escherichia coli* (*E. coli*) and *Staphylococcus aureus* (*S. aureus*) were both utilized in this study and the method described by Thian *et al.* [24] was adopted. Briefly, discs plates containing HAp and Zn-doped HAp were immersed in 2 ml of tryptone soya broth made up of 4 × 106 cells/ml in a 24-well plate prior to incubation for 7 days at 37 °C. 100 μl of the test solution was retrieved after the incubation period and serial dilution was carried out in order to obtain surviving colonies. Approximately 25 μl aliquot of the latter was measured and mixed with a tryptone soya agar in triplicate and incubation was done at 37 °C for the formation of the colony. Bacteria, which were adhered onto the surface of HAp and Zn-doped HAp discs were fixed with formaldehyde, sequentially dehydrated and vacuum-dried. Samples of pure HAp were used as negative controls.

2.6. Kinetics study of the release of Zn ions from Zn-HAp composite

The modified method used by Weilin *et al.* [25] was adopted for the Zn ions release study. Briefly, 15 mg of scaffold load with different percentage of Zn-HAp/cells were immersed in 10 mL of phosphate buffered solution (PBS) of solution pH of 7.4 at 37 °C under constant shaking in a temperature bath shaker. At a predetermined time intervals, 3 mL of the release medium were sampled out for Zn ions determination using inductively coupled plasma-optical emission spectroscopy (ICP-OES) using Optima 3200 RL (Perkin Elmer, CA, USA) instrument while replacing with the same volume of fresh phosphate buffered solution (PBS).

3. Results

3.1. XRD analysis

The phase stability, purity and the effects of incorporating Zn ions into apatite structure were examined by XRD and compared with JCPDS file no. 09–432 as indicated in Fig. 1. The pattern presents very broad peaks as a consequence of poor crystallinity. Changes in the peak intensity coupled with peaks broadening after the incorporation of the Zn ions were apparent. First, there were slight shifts in peak positions for all the Zn-doped HAp powder as compared with pure HAp. This observation was also corroborated by Gamal *et al.* [25] and it was assumed that the greater structural strain and smaller particle size in the Zn-doped HAp relative to pure HAp may be responsible for this phenomenon. Except for the case of the pure HAp and 5%Zn + HAp, the appearance of peaks in the XRD spectra at 2θ = 10. 46° and 26.16° corresponding to the (200) and (220) planes showed the presence of a new phase called parascholzite ($CaZn_2(PO_4)_2.2H_2O$) also known as calcium zinc phosphate in the apatite lattice. Within the Zn ion incorporation onto the HAp lattice, the intensity of the peak corresponding to the plane (200) increased significantly up to 15% Zn-HAp, while that of the HAp at (211) plane decreased and became broad with increasing Zn concentration. Fumiaki *et al.* [22] observed that a rise in Zn fraction increases the peak intensity of the parascholzite, while that of the apatite reduces with the apatite disappearing at 70 mol% Zn. In this study, however, it was observed that the disappearance of HAp was noticed at 20 mol% of Zn incorporation. With a decrease in the peaks intensity at higher Zn^{2+} incorporation, the crystallinity of the apatite decreases drastically at higher contents of Zn^{2+} in the lattice. LeGeros [26], reported the inhibitory effect of Zn^{2+} on HAp formation with a reduction in the crystallinity of the apatite. The importance of this observation is that the incorporation of Zn^{2+} onto the apatite resulted in crystal defects in the crystal structure and the crystal becomes more defective. The unit cell parameters (a and c), as well as the unit cell volumes (V), were computed to evaluate further the lattice defects caused by the substitution of Zn^{2+} onto the structure of the HAp and they are as presented in Table 1 [22, 26, 27].

On comparing the parameters of the Zn-doped apatite with the standard value for HAp (using JCPDS no. 09–432), it was observed that their values appeared smaller. The lattice parameter 'a' increased on increasing the concentration of Zn ions adsorbed onto the structure of the apatite up to 20% Zn, while on the contrary, the lattice parameter 'c', as well as the unit cell volume, showed a drastic decrease on increasing Zn ions onto the apatite surface. Reports in literature had it that since the ionic radius of Zn^{2+} (0.074 nm) is smaller than that of Ca^{2+} (0.099 nm), the replacement of Ca ions by Zn ions resulted to some defects in either or

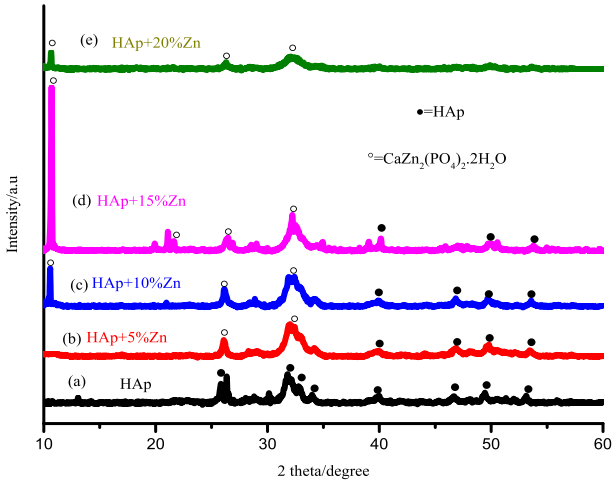

Fig. 1. XRD spectra of HAp and Zn-HAp composite.

Table 1
Lattice parameter of pure HAp and Zn-doped HAp.

Samples	FWHM (°)	Parameters			Crystallite size (nm)
		a (nm)	c (nm)	V (nm^3)	
HAp	0.0816	0.9373	0.6887	1.565	68
5%Zn + HAp	0.1224	0.9422	0.6855	1.575	60
10%Zn + HAp	0.1632	0.9387	0.6829	1.557	57
15%Zn + HAp	0.2040	0.9397	0.6854	1.566	45
20%Zn + HAp	0.33416	0.9509	0.6836	1.600	41

both lattice parameters [28, 29]. According to LeGeros and LeGeros [30], the substitution of Zn ions for Ca sites in HAp lattice causes an expansion in the lattice parameters 'a' and 'c' simultaneously. On the contrary, Fumiaki *et al.* [22] reported an increase in the lattice parameter 'a' and reduction in lattice parameter 'c' on increasing the concentration of Zn incorporated into the apatite and reported the limit of Zn that can be substituted for Ca sites in the apatite as 15 mol%. While the latter is in conformity with this present work, the formal is however contrary. Also, in this present work, the limit of Zn that can be substituted for Ca sites were observed to be 5% after which the appearance of the parascholzite phase was noticed. The defects in the lattice structure as a result of the incorporation of Zn ions into HAp lattice caused shrinking to the HAp crystal. A similar phenomenon of lattice parameter contraction was reported in previous work for cations having smaller ionic radius than Ca such as (Fe^{2+}, Zn^{2+},Mg^{2+}, Y^{3+}, In^{3+}), while lattice parameters expansion was reported for cations with larger ionic radius than Ca such as (La^{3+}, Bi^{3+}) [22, 31]. Various explanations have been provided in the literature on the mechanism of lattice defects in the crystal lattice of HAp due to the incorporation of metal ions. Borum-Nicholas and Wilson [32] and which was also corroborated by Ofudje *et al.* [33] reported that the replacement of carbonate anion for the phosphate anion can result into an increase along the c-axis and a contraction along the a-axis in the unit cell length. On the other hand, the replacement of carbonate by hydroxyl group causes an increase along the a-axis and a reduction in the c-axis. This observation agrees well with the findings of this work in the case of pure HAp. The possibility for the introduction of HPO_4^{2-}, CO_3^{2-}, H_2O, and others into the apatite during synthesis from precipitation method leading to Ca-deficient apatite which can cause some defects (expansions) in the lattice parameters 'a' and 'c' was reported by LeGeros and LeGeros [30]. The substitution of H_2O for –OH sites in apatite is known as "lattice H_2O" [21]. In this present work, it is evident from FT-IR analysis that the possibility of the effect of the incorporation of HPO_4^{2-} and CO_3^{2-} for Zn-doped HAp is not feasible since their presence in the apatite were not observed. Thus, a factor which could be responsible for the lattice defects was assumed to be adsorption of lattice H_2O coupled with the incorporation of Zn ions into the lattice. However, since the defect increases with the Zn ions concentration, it is assumed that the substitution of Zn ions into HAp structure caused the lattice parameters defects. The values of the crystallite sizes computed from the XRD data using the Scherrer's formula are as presented in Table 1. The peak from (002) reflection planes was adopted in calculating the crystallite size. The crystallite size ranged from 68 nm in pure HAp to 41 nm in 20%Zn-doped HAp showing a decrease in the crystal size of all Zn-doped HAp samples as compared with pure HAp. This, of course, is expected due to the broadening of the peaks as indicated in the XRD chart in Fig. 2. This may be due to the smaller ionic radii of zinc which is the basis for the HAp structure shrinking [23, 30]. Fig. 2 depicts the XRD of Zn-HAp nanocomposite sintered at 1000 °C, the spectra showed many sharp peaks corresponding to HAp which indicated high crystallinity after sintering. The effects of temperature on the lattice parameters were also evaluated and the results are as presented in Table 2. The lattice parameter 'a' increases with Zn

Table 2
Lattice parameter of pure HAp and Zn-doped HAp at heating at 1000 °C.

Samples	FWHM (°)	Parameter			Crystallite size (nm)
		a (nm)	c (nm)	V (nm^3)	
5%Zn + HAp	0.117	0.9393	0.6861	1.567	75
10%Zn + HAp	0.1004	0.9409	0.6855	1.571	87
15%Zn + HAp	0.1171	0.9411	0.6854	1.573	76
20%Zn + HAp	0.1004	0.9415	0.6852	1.573	87

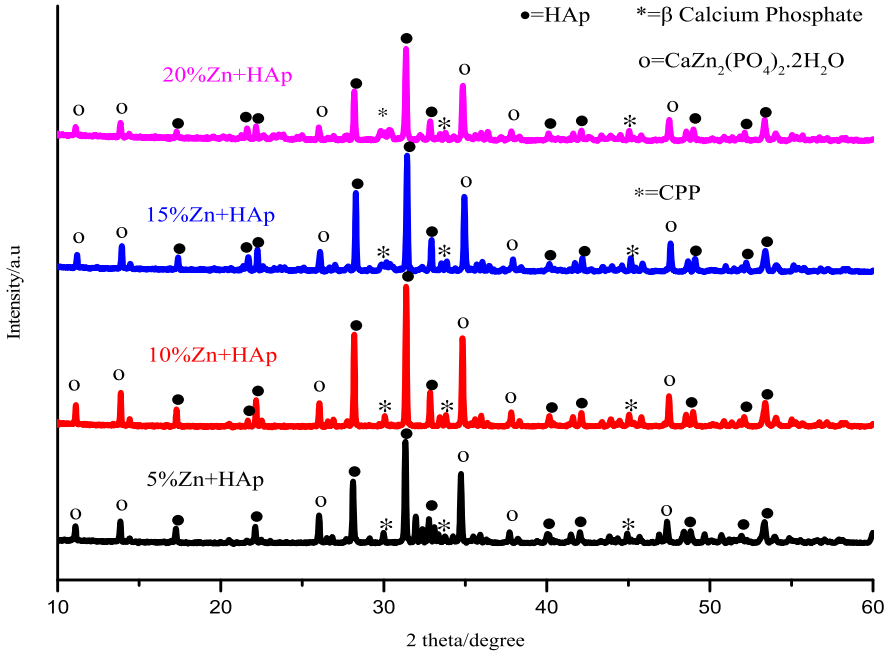

Fig. 2. XRD spectra of Zn-HAp composite after sintering at 1000 °C.

ion concentration while lattice parameter 'c' decreases with increase Zn ion concentration. The crystallite sizes drastically increased indicating better crystallinity. Zn incorporation inhibits the growth of HAp in co-precipitation, high temperature is needed to insert the Zn ion particles into the HAp structure which is in accordance with the study of Gomes *et al.* [30] who argued that majority of the Zn ion didn't absorb into the crystal structure of hydroxyapatite until after sintering over 1000 °C. In the absence of lattice H2O at higher temperature due to evaporation, Zn ions with smaller ionic radii occupy the Ca ion sites [22, 27]. An only a small amount of β-calcium phosphate was observed in the entire Zn-doped sample which is an indication that the substitution of Zn into the HAp lattice stabilized the apatite structure.

3.2. FT-IR studies

The FT-IR spectra of the prepared apatite with various Zn-doped HAps are as presented in Fig. 3, while the values of the bands are as presented in Table 3. Main characteristic bands of hydroxyapatite were observed for all samples with little variations in absorption bands indicating the substitution of Zn ions into the apatite structure. The peaks corresponding to PO_4^{3-} and –OH became broadening on increasing the concentrations of Zn fraction and this reduced the crystallinity of the apatite as observed in XRD analysis. The bands in the range of 562–564 cm^{-1} were attributed to O–P–O bending (v4), while those between 1036 and 1048 cm^{-1} correspond to the asymmetric stretching mode of PO_4^{3-} (v3). The peaks observed between 1387 and 1389 cm^{-1} indicated the presence of $–NO_3^-$ groups from the synthesis starting material. Similarly, the broad bands around 3409–3466 cm^{-1} were assigned to the N–H groups from the synthesis precursor. The peaks observed at 889 cm^{-1} is as a result of the presence of CO_3^{2-} adsorbed during the synthesis process from open air. It should be noted that the peak at 889 cm^{-1} in the pure HAp was not observed in all the Zn-doped HAp which is an indication that the incorporation of Zn ions into the apatite replaces the carbonate group in the pure HAp synthesized via co-precipitation method along the c-axis. This is in accordance with the results obtained from the XRD analysis where the carbonated group appeared to have been replaced by the incorporation of Zn ion into the apatite leading to a reduction in the lattice parameter 'c' and a rise in lattice parameter 'a' of the apatite. The bands between 1645 and 1665 cm^{-1}, 3137 and 3144 cm^{-1} were assigned to adsorbed water molecules, while those appearing between 3523 and 3621 cm−1 were allotted to the O–H stretching. FT-IR spectra of Zn-doped HAp which was sintered at 1000 °C is as presented in Fig. 4, while the values of the bands are as presented in Table 4. Decrease or total removal of –OH peaks at higher temperature suggests dehydroxylation. Ito *et al.* [15] reported that Zn-substituted apatite changes to Zn-substituted β-TCP after sintering at 800 °C. It was however observed that peaks corresponding to pure HAp and parascholzite were prominent in all the zinc-doped HAp which is in good conformity with XRD results. The major peaks present in the apatite were ascribed to the phosphate group. After heat treatment, the appearance of triplet phosphate peaks at 430, 546 and 603 cm^{-1} became prominent. The presence of the peaks corresponding to CO_3^{2-} and NO_3^- groups were absent after heat treatment. This is an indication that they were removed as volatile gases at a higher temperature.

Table 3
FT-IR of pure HAp and Zn-doped HAp.

HAp	5%Zn + HAp	10%Zn + HAp	15%Zn + HAp	20%Zn + HAp	Functional group assignment (cm^{-1})
564	564	564	562	563	O–P–O bending (υ_4)
889	–	–	–	–	CO_3^{2-}
1036	1040	1039	1041	1047	Asymmetric stretching mode PO_4^{3-} (υ_3)
1389	1388	1389	1387	1388	NO_3^- group
1645	1665	1661	1660	1646	Adsorbed H_2O
3157	3141	3137	3142	3144	Adsorbed H_2O
3453	3466	3409, 3447	3411, 3466	3415	N–H stretching
3602	3621	3525, 3609	3523, 3618	3516	O–H stretching

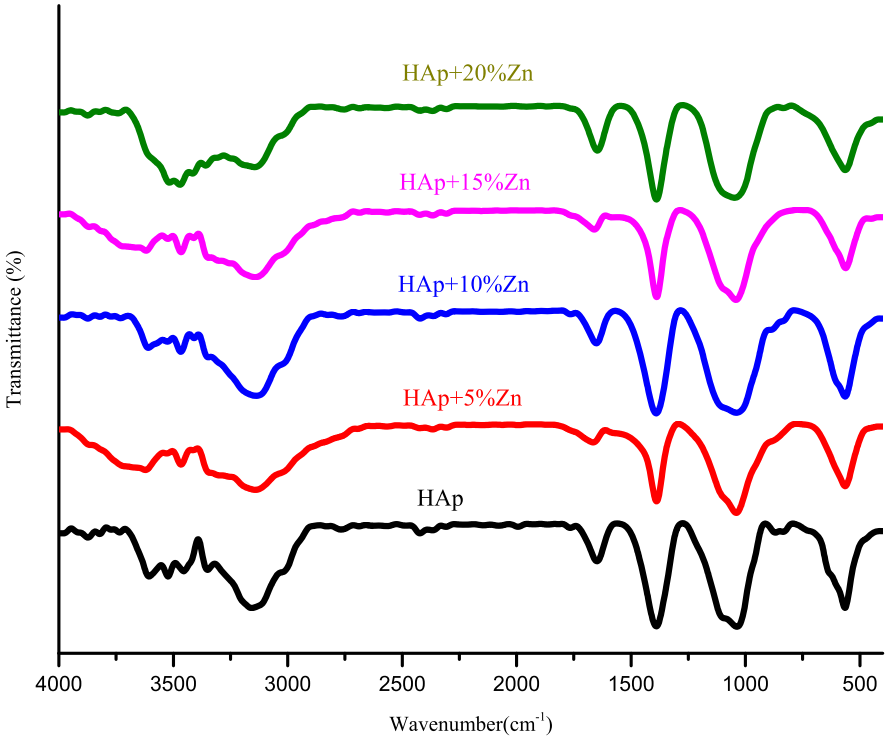

Fig. 3. FT-IR spectra of HAp and Zn-HAp composite.

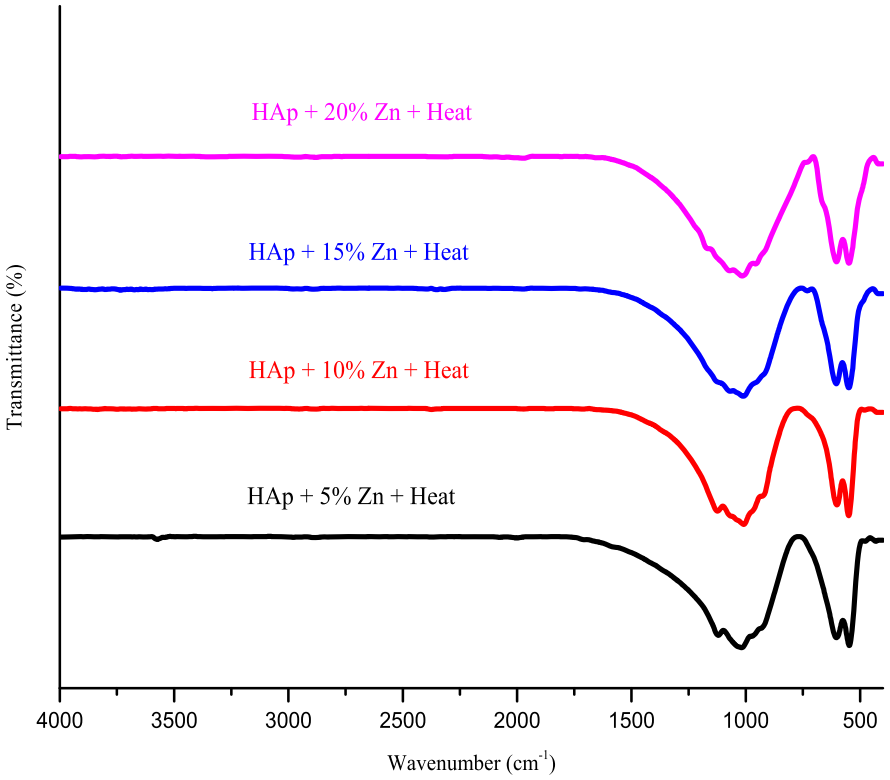

Fig. 4. FT-IR spectra of HAp and Zn-HAp after sintering at 1000 °C.

Table 4
FT-IR of Zn-doped HAp after sintering at 1000 °C.

5%Zn + HAp	10%Zn + HAp	15%Zn + HAp	20%Zn + HAp	Functional group assignment (cm^{-1})
430	–	–	–	PO_4^{3-} bending (υ_2)
546	549	548	548	O–P–O bending (υ_4)
603	601	603	603	O–P–O bending (υ_4)
1017	1008	1010	1015	Asymmetric stretching mode PO_4^{3-} (υ_3)
1119	1122	–	–	Asymmetric stretching mode PO_4^{3-} (υ_3)
3574	–	3738	–	O–H stretching

3.3. SEM and TEM analyses

The morphologies of the synthesized HAp and Zn-doped HAp before and after sintering are presented in Fig. 5 while the TEM micrograph analyses with their corresponding SAED pattern as inserted are presented in Fig. 6. The SEM analysis showed fine particles with a nearly round shape and interconnected pores were observed. These interconnected pores can be very useful in promoting tissue growth during bone implants [34]. The result revealed that as-prepared HAp contains needle-like nanocrystals of length varying from 15 to 35 nm and width varying from 4 to 12 nm. These needle-like crystals grow to form round particulate morphology after the substitution of zinc ions into the structure of apatite.

3.4. Density and elemental analyses

EDAX investigation of prepared biomaterials are as presented in Fig. 7 (a and b). The presence of Ca, P, O, and Zn were observed after the insertion of Zn ions into the apatite. This showed that Zn ions were substituted into the apatite. The ratio of Ca/P of the pure HAp was found to 1.67. After the insertion of Zn ions, the Ca/P decreases gradually as shown in Fig. 7c. This decrease in the ratio of Ca/P might be due to the decrease in the contents of Ca in the lattice of the apatite since Zn ions might have substituted the Ca ions on increasing the concentration of the dopant. However, the incorporation of Zn ions into the HAp can act as an anti-microbial, stimulate bone formation, and slow osteoblast resorption [35]. The density of the synthesized Zn-HAp nanocomposite evaluated is as presented in Fig. 7b. The densities were found to range from 2.34 to 2.77 g/cm^3 in as-synthesized HAp and from 2.57 to 2.96 g/cm^3 in sintered Zn-doped HAp samples. In both cases, the densities of the Zn-HAp nanocomposite were observed to be higher than the pure HAp. The densities of the Zn-doped apatite increase with Zn ion concentration which can be due to the ionic exchange in the HAp structure leading to structural defects [4, 36].

3.5. XPS analysis

Fig. 8 shows the XPS spectra of Zn doped HAp. The spectra showed the presence of calcium (Ca2p), oxygen (O1s), phosphorus (P2p) and Zinc (Zn2P) peaks. This result further demonstrated that the as-prepared apatite contained the presence of zinc ions. The results of this research work are in agreement with literature reports [18, 24].

3.6. TGA analysis

Thermal stability of pure HAp and 10%Zn-HAp composite obtained by means of TGA under nitrogen environment in the temperature range of 25–1000 °C are as presented in Fig. 9a and b respectively. A total mass loss of 3.26 % observed in the pure HAp was attributed to the removal of adsorbed water at a temperature below 200 °C, dehydration of hydroxides in the temperature range of 380–450 °C, and elimination of surface carbonate-like groups observed in the range of 450–850 °C. This is in accordance with literature reports for pure HAp powders [37]. On the other hand, Zn-doped HAp showed higher mass loss of 7.22 % between 25 and 800 °C which could be attributed to the elimination of adsorbed water (0–350 °C), dehydration of Zn hydroxides (350–600 °C), and decomposition of carbonate-like groups which corroborate the FT-IR

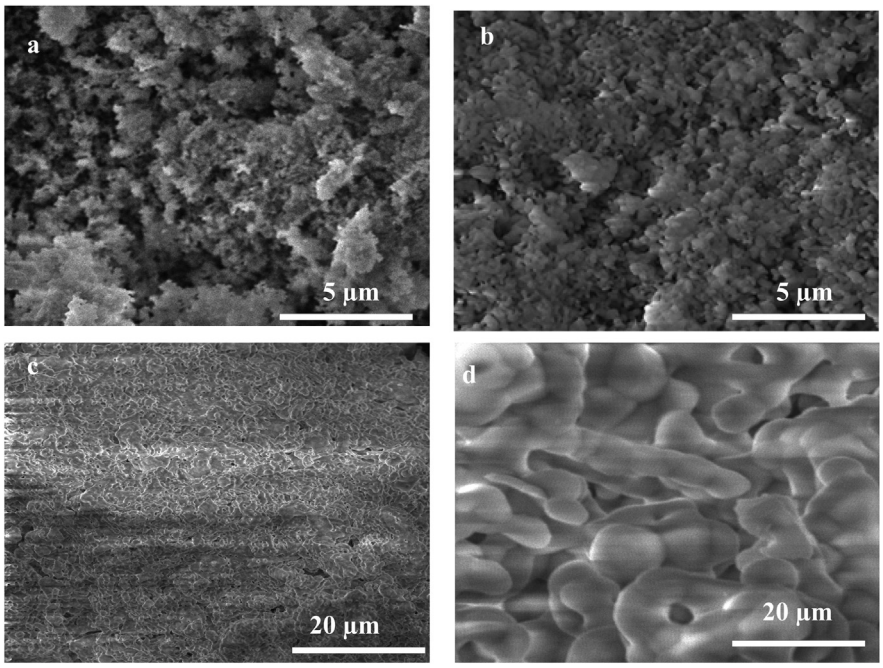

Fig. 5. SEM images of (a) HAp (b) sintered HAp at 1000 °C, (c) 10%Zn + HAp and (d) sintered 10%Zn + HAp at 1000 °C.

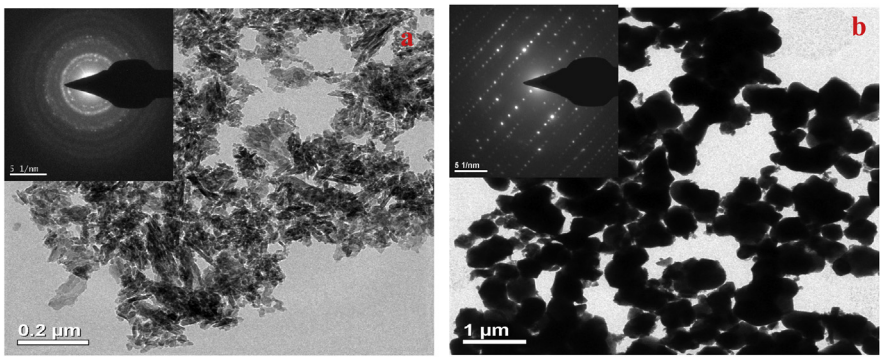

Fig. 6. TEM images of (a) HAp and (b) 10%Zn-HAp with their corresponding SAED as inserted.

results (600–850 °C). Unlike the pure HAp, the Zn-doped showed no appreciable weight loss above a temperature of above 850 °C. This inferred the thermal stability of the Zn-doped apatite over the undoped HAp nanocomposite in the thermogravimetric study. It was also observed that the introduction of Zn ions into the apatite increased weight loss. Hyehyun *et al.* [38] observed that since the boiling point of HAp is much higher than that of Zn, more weight loss occurs on Zn substituted HAp. This is in line with what was observed in this present study.

3.7. *In vitro* bioactivity study

Fig. 10a, b, c shows the image of prepared HAp, pellets Zn-doped HAp, and Zn-HAp-AMB composites after sintering at 1000 °C. Presence of pores on the surface of the nano-composite was obvious. It can be seen that the interface between the HAp and the AMB leads to the formation of interconnected porous within the scaffold structure. Fig. 10d represents the plot of mercury porosimeter of Zn-doped HAp scaffold with pore diameters in the range of 15–100 µm. An increase in the weight percent of the ammonium bicarbonate (AMB) was found to have increased the porosity of the granules as illustrated in Fig. 11a. The density of the nanocomposite decreases with an increase in the percentage weight of AMB and this could be as a result of the fact that the theoretical density of AMB (1.586 gcm^{-1}) is smaller than that of the pure HAp (3.15 gcm^{-1}). The entire sample tested demonstrated significant porosities with 35 %–70 % for 10 wt% and 50 wt% AMB composite apatite respectively. In order to maintain a good mechanical property of the composite, ammonium bicarbonate of 40 wt% with a porosity of 50 % was chosen. Esen and Bor [39], opined that the minimum porosity of macropores should be 55 % for direct connectivity which would leads to interconnected porous structure and thus improve the ingrowth of cell in the scaffold as well as transport of metabolic products.

Fig. 12 shows the SEM images of (a) scaffold Zn/HAp showing the formation of interconnected porous structure (b & c) Zn/HAp scaffold after immersion in SBF solution. The image showed the growth of apatite on the surface of the porous scaffold, especially around the porous regions. A careful look at the SEM of the SBF treated scaffolds reveal that most of the porous area were covered by apatite layer after 3 days of SBF treatment and almost covered after 7 days of immersions respectively. The spherical deposition of apatite layer on the surface of the scaffold cross-checked through FT-IR of the SBF soaked HAp scaffold as showed in Fig. 13.

The FT-IR spectra show the presence of –OH stretching bands of the apatite structure at 3600 cm^{-1}, 3450 cm^{-1}, and 1650 cm^{-1}. The bands appearing at the range of 1086 to 1040 cm^{-1} are assigned to the stretching modes in the PO_4^{3-} group [40]. After SBF treatment, the FT-IR spectra showed some shift in peaks position at the carbonate, phosphate

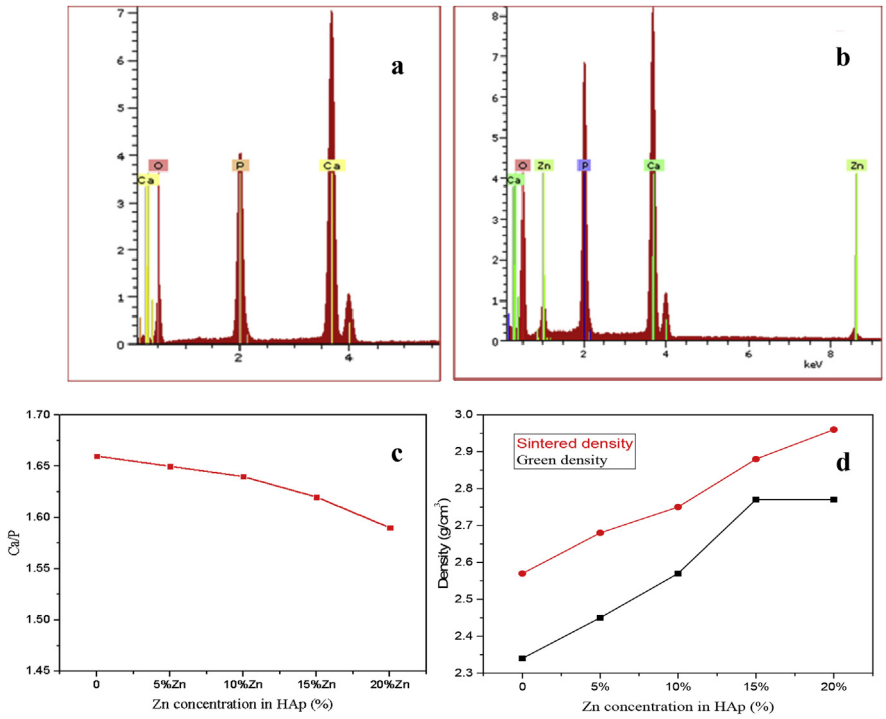

Fig. 7. EDAX of (a) pure HAp, (b) Zn-HAp nano composite, (c) Ca/P ratio and (d) green and sintered densities of Zn-HAp nano composite against Zn concentration.

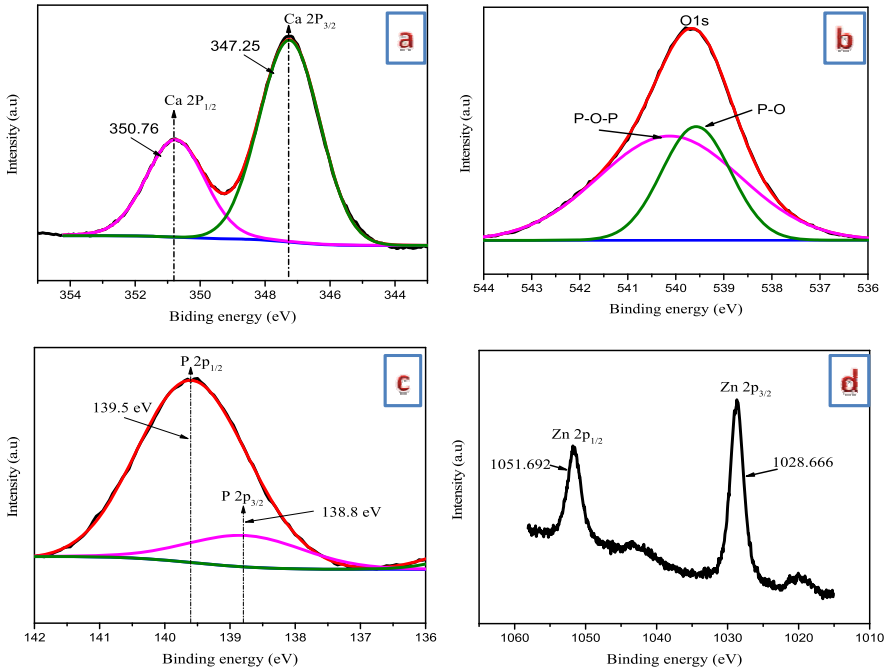

Fig. 8. XPS spectra of 10%Zn-HAp nano composite showing the devolution of biding energies of (a) calcium, (b) oxygen and oxygen-phosphorous, (c) phosphorous, and (d) zinc.

and hydroxyl groups. The characteristic of carbonate bands observed indicates that the crystal particles formed on the surface of the apatite incubation in SBF are attributed to the carbonated apatite which is similar in composition to the natural apatite. Thus, the combination of SEM and FT-IR study confirms the bioactivity of the scaffold. Pradnya *et al.* [41] reported that when a material is immersed in SBF solution, the formation of apatite layer on the surface of pellet goes through a sequence of chemical reactions such as nucleation, the growth of calcium phosphate, and spontaneous precipitation. It was further reported that the surface chemistry plays a significant role in this process and that the functional groups present on the scaffold materials also have a vital effect on the bone bonding property. The –OH and PO_4^{3-} groups are responsible for the formation of negative ions on the surface of the apatite, while Ca^{2+} ions form the positive group [39].

3.8. Antibacterial activity studies

The antibacterial activities of Zn-doped hydroxyapatite at different Zn

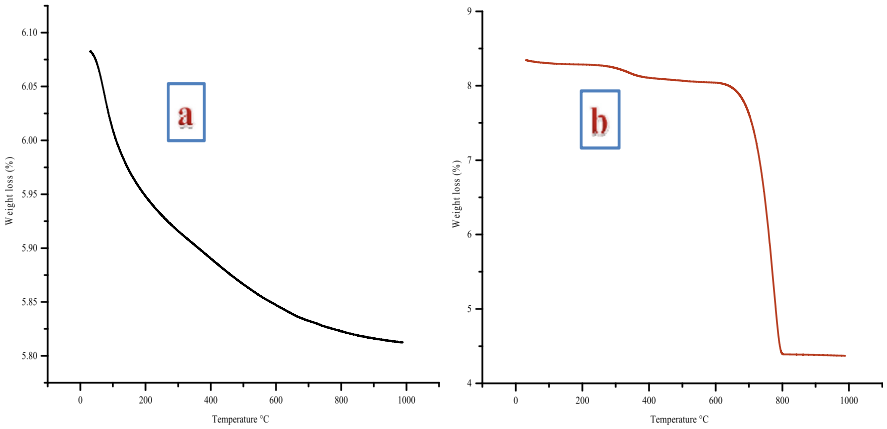

Fig. 9. TGA Analyses of (a) HAp and (b) 10%Zn-HAp nano composite at 1000 °C.

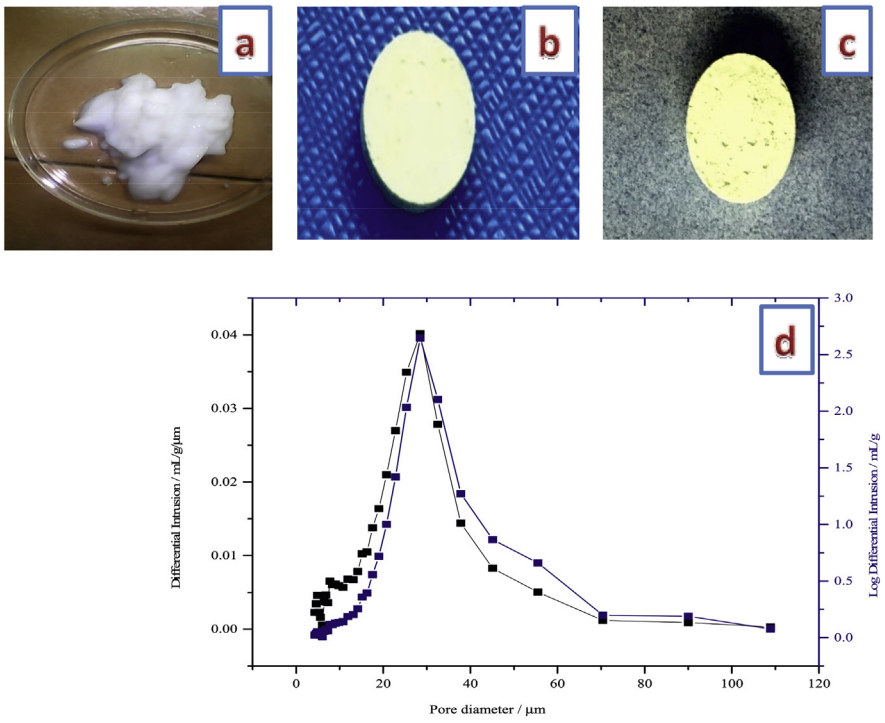

Fig. 10. Images of (a) HAp, (b) pellet of HAp (c) scaffold HAp-AMB composite after sintering at 1000 °C and (d) mercury porosimeter of HAp scaffold.

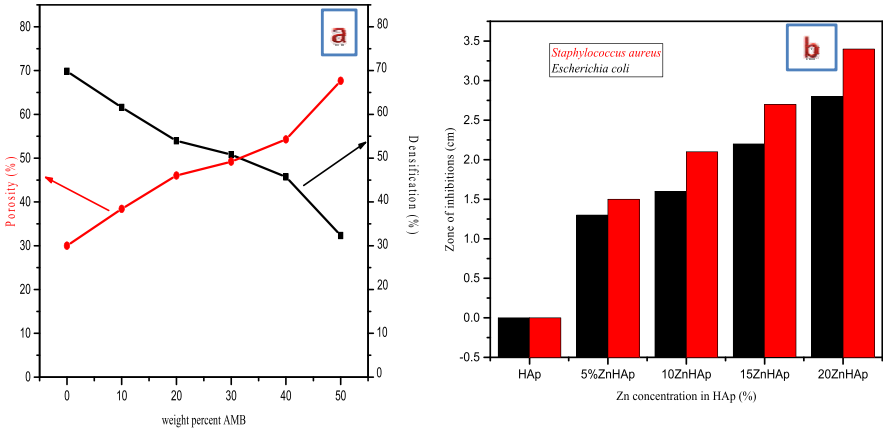

Fig. 11. Plots of (a) porosity and densification against weight percent and (b) zone of inhibition of HAp and Zn-doped hydroxyapatite at different Zn concentrations.

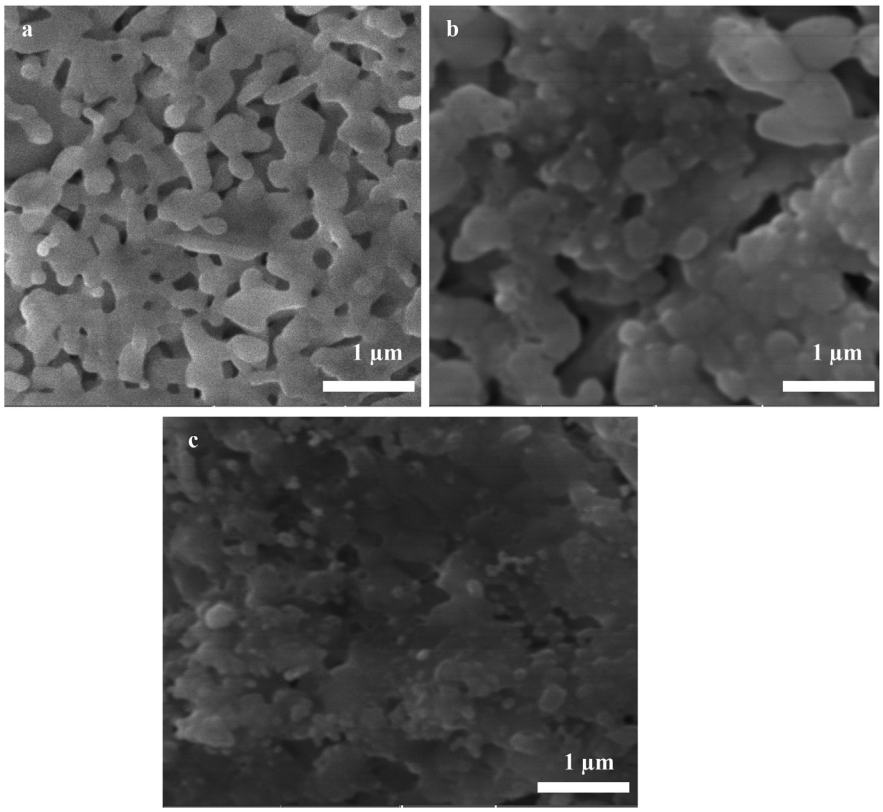

Fig. 12. SEM images of (a) 10%Zn/HAp scaffold, (b) 10%Zn/HAp scaffold after 3 days, and (c) after 7days of immersion in SBF solution at pH of 7.4 and temperature of 37 °C.

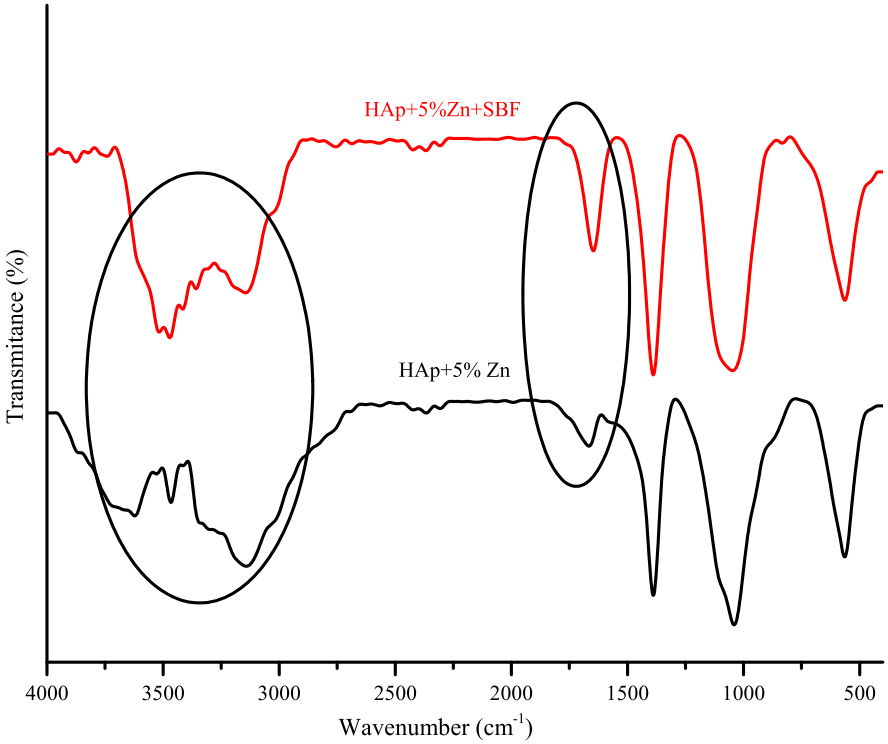

Fig. 13. FT-IR spectra of 10%Zn/HAp before and after immersion in SBF solution.

concentrations against different organisms were evaluated and are as shown in Fig. 11b. For the pure HAp (i.e 0 % ZnHAp), no zone of inhibition was observed indicating that the apatite lacks antimicrobial activity. However, all the Zn-doped HAp showed the zones of inhibitions which increased with the Zn ions concentrations in the apatite with the 20 % of Zn-doped HAp having the highest zone of inhibitions. Since the

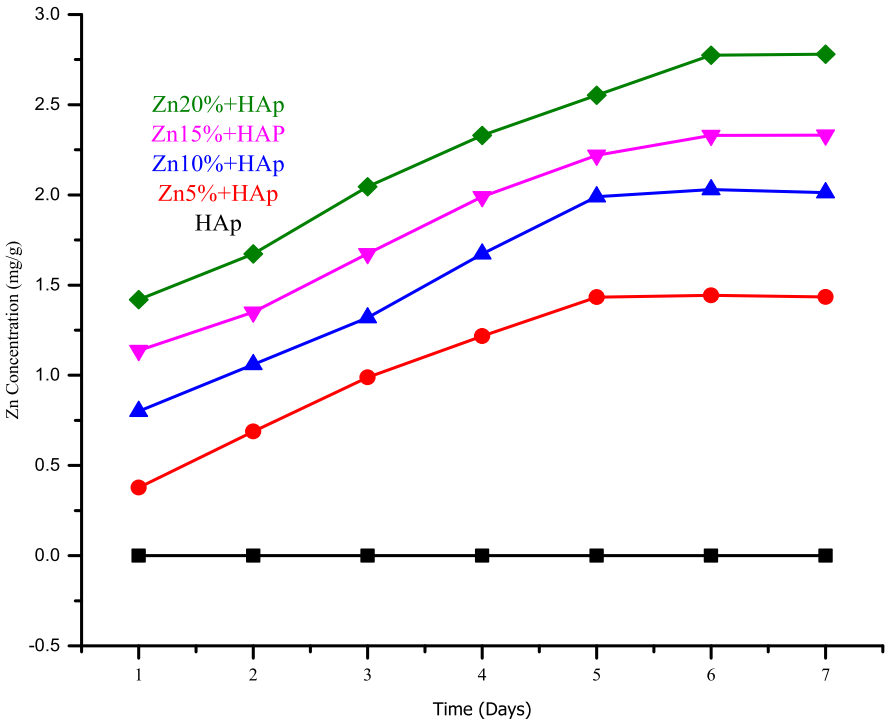

Fig. 14. Kinetics study of the release of Zn ions from Zn-HAp composite at a solution pH of 7.4 and temperature of 37 °C.

crystallinity of the HAp decreased with increase in the percentage of Zn ions concentrations in the apatite, the surface area of the apatite increases leading to the formation of bonds with the microorganisms which resulted in the death of the cell [40, 42]. Stanic *et al.* [19] proposed an antibacterial mechanism of Zn-doped HAp to be the formation of strong surface bonds between the HAp nano-composite with imidazole, thiol, carboxyl, and amino groups on the surface of the microorganism as a membrane of proteins, which leads to changes in the structure. It was reported further that permeability of the structurally changed microorganism membrane shows a significant increase, thus rendering the microorganism cells inept of properly regulating movement across the plasma membrane, and resulting in the death of the cell.

3.9. Kinetics study of the release of Zn ions

The release profile of Zn ions in phosphate buffered solution at 37 °C is shown in Fig. 14. It was observed that all the Zn-HAp/cell scaffolds exhibited release ability of Zn ions in PBS. The release of Zn ions from the Zn-HAp/cell was rapid within the first three days of immersion. However, as reaction time proceeded, the amount of Zn ions release from the surface of the cell load scaffold became slower and finally, no appreciable release was observed after five days of immersion as the reaction approached equilibrium [25]. The maximum amount of Zn ions released by 5%Zn-HAp, 10%Zn-HAp, 15%Zn-HAp and 20%Zn-HAp were 1.434, 2.012, 2.331, and 2.780 mg/g respectively. Also, it was noted that the amount of Zn ions released increased with the amount of Zn ions present in the Zn-HAp/cell load scaffolds. The rate of dissolution of HAp nanocomposite in the buffer solution at a solution pH of 7.4 is a function of their crystallinity as their rate of dissolution increases with a decrease in their crystallinity [43]. From this current study, the release rate of Zn doped HAp composite was in the order of 20%Zn-HAp > 15%Zn-HAp > 10%Zn-HAp > 5%Zn-HAp respectively and this is because the more the amount of Zn ions present on the HAp, the least crystalline the structure becomes as indicated in the XRD analysis which will then dissolve at a higher rate in phosphate buffer solution. On the contrary, the least Zn doped HAp showed slower release rate due to their higher crystallinity which enables them to dissolve at a slower rate in phosphate buffer solution.

4. Conclusion

In this work, Zn-doped hydroxyapatite composite was synthesized through chemical precipitation. Our findings revealed that zinc ions were successfully substituted into the HAp structure which caused a decrease in the crystallite size of the HAp with an increase in zinc ions concentrations. Similarly, lattice parameters varied with zinc ions concentrations which subsequently caused shrinking of the apatite structure. EDAX measurement showed a gradual decrease in Ca/P ratio suggesting the replacement of Ca with Zn ions resulting in the formation of Ca-deficient hydroxyapatite which could play a vital part in tissue engineering. The Zn-doped HAp–Zn composites showed excellent bioactive and antibacterial activity against *Staphylococcus aureus* and *Escherichia sp*.

Declarations

Author contribution statement

Edwin A. Ofudje: Conceived and designed the experiments; Performed the experiments; Analyzed and interpreted the data; Wrote the paper.

Abideen I. Adeogun: Conceived and designed the experiments; Performed the experiments, Wrote the paper.

Mopelola A. Idowu: Analyzed and interpreted the data; Contributed reagents, materials, analysis tools or data.

Sarafadeen O. Kareem: Contributed reagents, materials, analysis tools or data; Wrote the paper.

Funding statement

This work was supported by the Centre for Science and Technology of the Non-Aligned and Other Developing Countries (NAM S&T Centre), India.

Competing interest statement

The authors declare no conflict of interest.

Additional information

No additional information is available for this paper.

Acknowledgments

The authors are particularly grateful to CSIR-CECRI, Central Instrumentation Facility for their supports during characterization.

References

[1] M. Jarcho, Retrospective analysis of hydroxyapatite development for oral implant applications, Dent. Clin. N. Am. 36 (1992) 19–26.
[2] M.H. Fathi, A. Hanifi, Evaluation and characterization of nanostructure hydroxyapatite powder prepared by simple sol–gel method, Mater. Lett. 61 (2007) 3978–3983.
[3] R. Ramakrishnan, P. Wilson, T. Sivakumar, I. Jemina, A. comparative study of hydroxyapatites synthesized using various fuels through aqueous and alcohol mediated combustion routes, Ceram. Int. 39 (2013) 3519–3532.
[4] T.J. Webster, E.A. Massa-Schlueter, J.L. Smith, E.B. Slamovich, Osteoblast response to hydroxyapatite doped with divalent and trivalent cations, Biomaterials 25 (2004) 2111–2121.
[5] O. Kaygili, C. Tatar, The investigation of some physical properties and microstructure of Zn-doped hydroxyapatite bioceramics prepared by sol–gel method, J. Sol. Gel Sci. Technol. 61 (2012) 296–309.
[6] S. Samani, S.M. Hossainalipour, M. Tamizifar, H.R. Rezaie, In vitro antibacterial evaluation of sol-gel-derived Zn-, Ag-, and (Zn+Ag)-doped hydroxyapatite coatings against methicillin-resistant Staphylococcus aureus, J. Biomed. Mater. Res. A (2013).
[7] K. Kaviyarasu, A. Mariappan, K. Neyvasagam, A. Ayeshamariam, P. Pandi, P.R. Palanichamy, C.G. Gopinathan, T. Mola, M. Maaza, Photocatalytic performance and antimicrobial activities of HAp-TiO_2 nanocomposite thin films by sol-gel method, Surf. Interfaces 6 (2017) 247–255.
[8] K. Sóballe, S. Overgaard, E. Stender-Hansen, H. Brokstedt-Rasmussen, M. Lind, C. Bünger, A review of ceramic coatings for implant fixation, J. Long Term Eff. Med. Implant. 9 (1999) 131–151.
[9] G. Willmann, Material properties of hydroxylapatite ceramics, Interceram 42 (1993) 206–208.
[10] L. Fang, Y. Leng, P. Gao, Processing and mechanical properties of HA/UHMWPE nanocomposites, Biomater. 27 (20) (2006) 3701–3707.
[11] J.C. Huang, Y.J. Ni, Z.C. Wang, Preparation of hydroxyapatite functionally gradient coating on titanium substrate using a combination of electrophoretic deposition and reaction bonding process, Surf. Coating. Technol. 204 (21) (2010) 3387–3392.
[12] P. Parente, A.J. Sánchez-Herencia, M.J. Mesa, B. Ferrari, Functionalizing Ti-surfaces through the EPD of HA/NanoY_2O_3, J. Phys. Chem. B 117 (6) (2013) 1600–1607.
[13] C.B. Ustundag, O. Avciata, F. Kaya, C. Kaya, Hydrothermally mixed hydroxyapatite-multi wall carbon nanotubes composite coatings on biomedical alloys by electrophoretic deposition, J. Phys. Chem. B 117 (6) (2013) 157–1576.
[14] D. Lahiri, S. Ghosh, A. Agarwal, Carbon nanotube reinforced hydroxyapatite composite for orthopedic application: a review, Mater. Sci. Eng. C-Mater. 32 (7) (2012) 1727–1758.
[15] A. Ito, K. Ojima, H. Naito, N. Ichinose, T. Tateishi, Preparation, solubility, and cytocompatibility of zinc-releasing calcium phosphate ceramics, J. Biomed. Mater. Res. 50 (2000) 178–183.
[16] S. Miao, K. Cheng, W. Weng, P. Du, G. Shen, G. Han, W. Yan, S. Zhang, Fabrication and evaluation of Zn containing fluoridated hydroxyapatite layer with Zn release ability, Acta Biomater. 4 (2) (2008) 441–446.
[17] M. Yamaguchi, R. Yamaguchi, Action of zinc on bone metabolism in rats: increases in alkaline phosphatase activity and DNA content, Biochem. Pharmacol. 35 (5) (1986) 773–777.
[18] X. Wang, A. Ito, Y. Sogo, X. Li, A. Oyane, Zinc-containing apatite layers on external fixation rods promoting cell activity, Acta Biomater. 6 (3) (2010) 962–968.
[19] V. Stanić, S. Dimitrijević, J. Antić-Stanković, M. Mitrić, B. Jokić, I.B. Plećaš, S. Raičević, Synthesis, characterization and antimicrobial activity of copper and zinc-doped hydroxyapatite nanopowders, Appl. Surf. Sci. 256 (20) (2010) 6083–6089.
[20] K.A. Gross, L. Komarovska, A. Viksna, Efficient zinc incorporation in hydroxyapatite through crystallization of an amorphous phase could extend the properties of zinc apatites, J. Australas. Ceram. Soc. 49 (2) (2013) 129–135.
[21] V.M. Rusu, C.H. Ng, M. Wilke, B. Tiersch, P. Fratzl, M.G. Peter, Size- controlled hydroxyapatite nanoparticles as self-organized organic–inorganic composite materials, Biomater. 26 (2005) 5414–5424.
[22] M. Fumiaki, K. Yoshiteru, S. Yoko, Formation and structure of zinc-substituted calcium hydroxyapatite, Mater. Res. Bull. 40 (2005) 209–220.
[23] T. Kokubo, H. Takadama, How useful is SBF in predicting in vivo bone bioactivity? Biomater. 27 (2006) 2907–2915.
[24] E.S. Thian, T. Konishi, Y. Kawanobe, P.N. Lim, C. Choong, B. Ho, M. Aizawa, Zinc-substituted hydroxyapatite: a biomaterial with enhanced bioactivity and antibacterial properties, J. Mater. Sci. Mater. Med. 24 (2013) 437–445.
[25] Y. Weilin, S. Tuan-Wei, Q. Chao, D. Zhenyu, Z. Huakun, Z. Shichang, S. Zhongmin, Z. Ying-Jie, C. Daoyun, H. Yaohua, Evaluation of zinc-doped mesoporous hydroxyapatite microspheres for the construction of a novel biomimetic scaffold optimized for bone augmentation, Int. J. Nanomed. 12 (2017) 2293–2306.
[26] R.Z. LeGeros, References/subject index, in: Calcium Phosphates in Oral Biology and Medicine, vol. 15, Karger Publishers, 1991, pp. 172–201.
[27] G.A. Gamal, F.A. Al-Mufadi, A.H. Said, Effect of iron additives on the microstructure of hydroxyapatite effect of iron additives on the microstructure of hydroxyapatite, Eng. Technol. Appl. Sci. Res. 3 (6) (2013) 532–539.
[28] T.J. Webster, C. Ergun, R.H. Doremus, R. Bizios, Hydroxyl apatite with substituted magnesium, zinc, cadmium, and yttrium II: mechanisms of osteoblast adhesion, J. Biomed. Mater. Res. 59 (2002) 312–318.
[29] X. Chen, Q.L. Tang, Y.J. Zhu, C.L. Zhu, X.P. Feng, Synthesis and antibacterial property of zinc loaded hydroxyapatite nanorods, Mater. Lett. 89 (2012) 233–235.
[30] R.Z. LeGeros, J.P. LeGeros, Dense hydroxyapatite, Adv. Ser. Ceram. 1 (1993) 139–180.
[31] S. Gomes, J.-M. Nedelec, E. Jallot, On the effects of temperature on the insertion of zinc into hydroxyapatite, Acta Biomater. 8 (2012) 1180–1189.
[32] L. Borum-Nicholas, O.C. Wilson Jr., Surface modification of hydroxyapatite. Part I. *Dodecyl alcohol*, Biomater. 24 (21) (2004) 3671–3679.
[33] E.A. Ofudje, R. Archana, A.I. Adeogun, M.A. Idowu, S.O. Kareem, D.K. Pattanayak, Synthesis of organic derived hydroxyapatite scaffold from pig bone waste for tissue engineering applications, Adv. Powder Technol. (2017).
[34] B. Promita, B. Howa, C. Abhiji, K.N. Samit, Animal trial on zinc doped hydroxyapatite: a case study, J. Asian Ceram. Soc. 2 (2014) 44–51.
[35] M. Yamaguchi, H. Oishi, Y. Suketa, Stimulatory effect of zinc on bone formation in tissue culture, Biochem. Pharmacol. 36 (1987) 4007–4012.
[36] E. Landi, G. Logroscino, L. Proietti, A. Tampieri, M. Sandri, S. Sprio, Biomimetic Mg-substituted hydroxyapatite: from synthesis to in vivo behaviour, J. Mater. Sci. Mater. Med. 19 (2008) 239–247.
[37] A. Cotescu, I. Pasuk, F. Ungureanu, A. Dinischiotu, M. Costache, F. Huneau, S. Galaup, P. Le Coustumer, D. Predoi, Physico-chemical properties of nano-sized hexagonal hydroxyapatite powder synthesized by sol-gel, Dig. J. Nanomater. Bios. 5 (2010) 989–1000.
[38] K. Hyehyun, M. Sudip, B. Subramaniyan, M. Panchanathan, S.M. Madhappan, O. Junghwan, Optimized Zn-doped hydroxyapatite/Doxorubicin bioceramics system for efficient drug delivery and tissue engineering application, Ceram. Int. (2017).
[39] Z. Esen, S. Bor, Processing of titanium foams using magnesium spacer particles, Scripta Mater. 56 (2007) 341–344.
[40] A. Nouri, P.D. Hodgson, C. Wen, Biomimetic porous titanium scaffolds for orthopaedic and dental applications, in Biomimetics learning from nature, In-Tech, Rijek, Croatia, 2001, pp. 415–450.
[41] N.C. Pradnya, M.B. Manjushri, U.M. Ravindra, P.M. Megha, S.K. Rajendra, Study of nanobiomaterial hydroxyapatite in simulated body fluid: formation and growth of apatite, Mater. Sci. Eng. B 168 (2010) 224–230.
[42] L. Jun, D. Jianxun, D. Yanfeng, W. Xiaole, W. Junchao, C. Yiwang, Antibacterial zinc oxide hybrid with gelatin coating, Mater. Sci. Eng. C (2017).
[43] D. Sudip, B. Amit, B. Susmita, Zn and Mg doped hydroxyapatite nanoparticles for controlled release of protein, Langmuir 26 (7) (2010) 4958–4964.